RSC Advances

Superior destabilization effects of LiBH4 with the addition of nano-sized nickel ferrite NiFe2O4

Journal:	*RSC Advances*
Manuscript ID	RA-ART-09-2015-017893.R1
Article Type:	Paper
Date Submitted by the Author:	11-Sep-2015

Complete List of Authors:	Zhang, Jun; Institute for Advanced Materials and Technology, USTB, State Key Laboratory for Advanced Metals and Materials Li, Ping; Institute for Advanced Materials and Technology, USTB, State Key Laboratory for Advanced Metals and Materials Wan, Qi; General Research Institute for Nonferrous Metals, Energy Material & Technology Research Institute Zhai, Fuqiang; Universitat Politècnica de Catalunya - BarcelonaTech, Departament Física Aplicada, EETAC Volinsky, Alex; University of South Florida, Department of Mechanical Engineering Qu, Xuanhui; Institute for Advanced Materials and Technology, USTB, State Key Laboratory for Advanced Metals and Materials

Superior destabilization effects of $LiBH_4$ with the addition of nano-sized nickel ferrite $NiFe_2O_4$

Jun Zhang [a], Ping Li [a*], Qi Wan [b], Fuqiang Zhai [c], Alex A. Volinsky [d], Xuanhui Qu [a]

[a] State Key Laboratory for Advanced Metals and Materials, Institute for Advanced Materials and Technology, University of Science and Technology Beijing, Beijing 100083, China

[b] Energy Material & Technology Research Institute, General Research Institute for Nonferrous Metals, Beijing 100088, China

[c] Departament Física Aplicada, EETAC, Universitat Politècnica de Catalunya - BarcelonaTech, Castelldefels 08860, Spain

[d] Department of Mechanical Engineering, University of South Florida, Tampa FL 33620, USA

Abstract

Introduction of a secondary compound, known as destabilization, is an effective way to improve the desorption performance of $LiBH_4$. In this paper the effects of nano-sized nickel ferrite ($NiFe_2O_4$) on the hydrogen storage properties of $LiBH_4$, processed by high energy ball milling, are studied. Non-isothermal desorption results show that the onset and predominant dehydrogenation temperature of $LiBH_4$ + 9 mol% $NiFe_2O_4$ is 89 °C and 190 °C, respectively. This is 226 °C and 260 °C lower than the

* **Corresponding author**: **E-mail**: ustbliping@126.com(Ping Li) **Tel**: +86-10-62333981; **Fax**: +86-10-62333981; **Address**: State Key Laboratory for Advanced Metals and Materials, Institute for Advanced Materials and Technology, USTB, Beijing 100083, China

fusion and decomposition temperature of $LiBH_4$, respectively. Moreover, over 10 wt% hydrogen can be obtained by 500 °C heating, compared with 2.4 wt% for the as-received $LiBH_4$. Additionally, over 5 wt% hydrogen can be released at 300 °C within 20 minutes of isothermal desorption. From the X-ray diffraction results and the small area electron diffraction analysis, Fe_3O_4, NiB and Fe_3B, in situ formed between the reaction of $LiBH_4$ and $NiFe_2O_4$, act as the actual destabilization effects.

Keywords: Hydrogen storage, nanoparticles, ball milling, lithium borohydrides.

1. Introduction

Hydrogen, as an eco-friendly and renewable energy carrier, is considered to be an alternative fuel for powering future vehicles[1-3]. Since vehicles need compact, affordable and safe H_2 containment to satisfy commercial needs, conventional hydrogen storage methods, including high-pressure tanks or condensation into liquid[4], need to be modified to meet increasingly demanding requirements. Therefore, this motivation has inspired scientists to research innovative hydrogen storage systems. Solid hydrogen storage materials have recently emerged as a new solution[3]. Some complex hydrides, like alanates, amides and borohydrides, have recently attracted considerable attention for potential hydrogen storage due to high hydrogen reserve mass and light weight [5]. In particular, lithium borohydrides ($LiBH_4$), possessing a high volumetric and gravimetric hydrogen density of 121 kg H_2 m^{-3} and 18.5 wt% [2, 6], is highly desirable for on-board H_2 storage in fuel cell vehicles. However, unacceptable hydrogen desorption temperature [6] (starts at around 400 °C and releases

only half the hydrogen below 600 °C) and hash re-hydrogenation conditions [7] (at 600 °C under 350 bar H_2) inhibit its practical applications. Over the past decades, researchers around the world have attempted numerous methods, including reacting with metal hydrides [8-11], restricting its particle size [12-14] and doping with metals [15-18] etc., to improve the hydrogen storage properties of $LiBH_4$. Even though tremendous advances have been achieved, none of these approaches can simultaneously fulfill all of the revised US DOE's 2010 criteria [19] to date.

Oxides have been commonly reported to be an effective method to enhance the hydrogen storage behaviors of $LiBH_4$. The early application of oxides can be dated back to 2003, when Züttel et al. firstly mixed $LiBH_4$ with SiO_2 to lower the onset desorption temperature to 200 °C, nearly a reduction of 200 °C compared with the pure $LiBH_4$, accompanied with 2.3 wt% H_2[6]. Then in 2008, Yu et al. found that TiO_2 can significantly enhance the hydrogen properties of $LiBH_4$ (the initial dehydrogenation temperature at 150 °C and the majority liberation of H_2 below 220 °C), with the charge transfer between Ti and B. They also suggested that other metal oxides with variable oxidation states should also play a similar role[20]. After that in 2009, Yu et al. systematically investigated a series of oxides to find out that the order of destabilization effect for $LiBH_4$ was $Fe_2O_3 > V_2O_5 > Nb_2O_5 > TiO_2$. Though the improvements talked are encouraging, the primary desorption temperature is still too high. The reports discussed above, however, have given us a hint to search for

some novel oxides, especially some metal oxides with both variable valent as well as larger Pauling's electronegativity[21].

To the best knowledge of us, no studies have been reported on $LiBH_4$ doped with Ni ferrite oxide ($NiFe_2O_4$). Meanwhile, from Li's report[22], $NiFe_2O_4$ shows a remarkable improvements on $LiAlH_4$ with the in situ formed $LiFeO_2$ and Al-Ni compounds. Likewise, the destabilization effects of $NiFe_2O_4$ may also be applicable to $LiBH_4$ when considering that $LiBH_4$ has a similar performance with $LiAlH_4$. Also, Zhai et al. points out that $MnFe_2O_4$ has better effect than Fe or Mn oxides alone in improving the dehydrogenation properties of $LiAlH_4$[23]. Due to the fact that Ni has a larger Pauling's electronegativity than Mn, we ultimately added $NiFe_2O_4$ nanoparticles to investigate their effects on the dehydrogenation performance of $LiBH_4$ prepared by high energy ball milling in this work.

2. Experimental details

$LiBH_4$ (≥95% pure), purchased from Acros Organics, and $NiFe_2O_4$ (≥99.99% pure, 20 nm), synthesized by the auto-combustion process (details of the synthesis process were given in the previous report [24]), were utilized directly without any further purification. $LiBH_4$ doped with different mole ratios (3 mol%, 5 mol%, 7 mol%, 9 mol% and 11 mol%) of $NiFe_2O_4$ was ball-milled under argon atmosphere by using a QM-3B high energy mill (Nanjing NanDa Instrument Plant) at a rotating speed of 1200 rpm for 30 min. Two kinds of stainless steel balls with 4 mm and 8 mm diameters were added with a ball-to-powder weight ratio of 30:1. Typically, 2 g

mixture was sealed in the stainless steel vessel within a high purity argon atmosphere during milling. To avoid excess heating of the stainless steel vessel, there were 10 min intervals between each 5 min milling process.

The non-isothermal and isothermal desorption were measured by using the Sieverts-type pressure-composition-temperature (P-C-T) apparatus (General Research Institute for Nonferrous Metals, China). Typically, 0.5 g sample was loaded into a stainless steel vessel and then heated from room temperature (RT) to 500 °C at a heating rate of 5 °C min^{-1} under 0.001 MPa hydrogen pressure. It should be noted that the additional content was not taken into consideration when calculating the released hydrogen in order to make a comparison with the as-received $LiBH_4$. The phase structure of the samples after milling and dehydrogenation was examined by an MXP21VAHF X-ray Diffractometer (XRD with Cu Kα radiation, 40 kV, 300 mA), with the 2θ angle ranged from 10° to 90° with a scanning rate of 10° min^{-1}. The morphology and phase constitution of all samples after ball milling and desorption were observed by field-emission scanning electron microscopy (FESEM, ZEISS ULTRA55, Germany) and transmission electron microscopy (Tecnai G2 F30 S-TWIN, FEI, USA). Simultaneous differential scanning calorimetry and mass spectrometry (DSC-MS) experiments were conducted under 50 mL min^{-1} argon flow in a NETZSCH STA 449F3 Jupiter instrument connected to a mass spectrometer (MS, Hiden Analytical HPR-20 QMS sampling system) between 50 °C and 500 °C with a

heating rate of 5 °C min^{-1}. The samples were transferred to Al_2O_3 crucibles under argon atmosphere for the DSC-MS measurements. Fourier transform infrared spectroscopy (FT-IR) analysis of the samples were carried out by using Nexus 670 FT-IR spectrometer. The FT-IR spectra were recorded from 32 scans between 500 cm^{-1} and 3000 cm^{-1} with a spectral resolution of 4 cm^{-1}.

All samples handling were performed under strictly inert conditions (≥99.99% Ar atmosphere) in the glove box (Mikrouna, Super-750) equipped with oxygen/humidity sensors and recirculation system to avoid oxidation and moisture. Oxygen and H_2O levels were kept below 0.1 ppm.

3. Results and discussion

Fig. 1 shows the destabilizing effects of $NiFe_2O_4$ on $LiBH_4$ during non-isothermal desorption. Overall, a decrease in the onset dehydrogenation temperature and significant advance in desorption kinetics occur with the $NiFe_2O_4$ doping compared with the as-received $LiBH_4$. Especially, the $LiBH_4$ + 9 mol% $NiFe_2O_4$ sample has an outstanding reduction in the onset desorption temperature, approximately at 89 °C, which is 226 °C lower than the as-received $LiBH_4$. This shows an advance compared with previous literature reports [13, 25]. Moreover, it eventually liberates 10.75 wt% hydrogen, compared with merely 2.4 wt% for the as-received $LiBH_4$. Notably, 6.6 wt% hydrogen can be obtained below 250 °C, whereas there is no apparent hydrogen release until 300 °C in the pristine $LiBH_4$. It seems that the ball milling has less effect

on improving the dehydrogenation performance of $LiBH_4$, as only 1.2 wt% more hydrogen liberated than the as-received $LiBH_4$ and the initial release temperature is nearly unchanged. It can be seen from the other curves in Fig. 1 that the initial temperature falls to 136 °C, 116 °C and 88 °C for the $LiBH_4$ + 3, 5, 7 mol% $NiFe_2O_4$ samples, respectively. Similarly, the actual hydrogen storage capacity continues to grow, reaching 4.09, 8.52, and 10.84 wt%. On the other hand, there is one exception when the addition amounts up to 11 mol%, the destabilizing effect discussed above is less pronounced, with the onset temperature of 130 °C and 7.11 wt% of hydrogen. The rise of the initial dehydrogenation temperature and the loss of capacity may be because of excessive $NiFe_2O_4$ addition leading to the first dehydrogenation stage occurring during the ball milling process.

Considering kinetic properties and hydrogen capacity, the 9 mol% $NiFe_2O_4$ addition sample is used to analyze the destabilization effect of $NiFe_2O_4$ in the following tests.

Parallel to the non-isothermal analysis, the desorption kinetics at constant temperature and dynamic vacuum are also explored. The desorption characterization of the as-milled $LiBH_4$ is performed under the same conditions for comparison. As indicated in Fig. 2, owing to the sluggish kinetics of $LiBH_4$, the as-received $LiBH_4$ can only release 1.46 wt% hydrogen in the first 60 seconds at 300 °C and after 12 minutes the final desorbed hydrogen is merely 1.69 wt%. It is notable that after doping with 9 mol% $NiFe_2O_4$, the content of desorbed hydrogen can increase to 2.74 wt% and the ultimate

hydrogen obtained is 5.49 wt% within 20 minutes. To further review this prominent effect, the temperature is lowered to 200 °C. Within 12 minutes, dehydrogenation capacity of 2.48 wt% is achieved for the $LiBH_4$ + 9 mol% $NiFe_2O_4$ sample. These results demonstrate the $NiFe_2O_4$ superiority in enhancing the $LiBH_4$ dehydrogenation kinetics compared with previous literature reports[26, 27].

The difference of the hydrogen capacity at the same temperature in the isothermal and non-isothermal hydrogen dehydrogenation should be ascribed to the hydrogen pressure during desorption process, as the isothermal desorption is conducted in the dynamic vacuum and the non-isothermal at hydrogen pressure of 0.001 MPa. In other words, the external hydrogen pressure may influence hydrogen liberation [28]. Both the non-isothermal and isothermal desorption results suggest that $NiFe_2O_4$ can significantly improve the dehydrogenation performance of $LiBH_4$.

To reveal the reaction mechanism in the desorption process, simultaneous differential scanning calorimetry and mass spectrometry (DSC-MS) measurements are carried out. In the case of pristine $LiBH_4$, there are three distinct endothermic signals at 114 °C, 285 °C and 428 °C, corresponding to orthorhombic to hexagonal structure transformation, fusion and decomposition of $LiBH_4$, respectively. MS results show that a small amount of hydrogen is released at 285 °C and a rapid dehydrogenation is observed at 428 °C, which is in agreement with the literature data [26, 29, 30]. Although

there was report[31] showing that downsizing may have dramatic effects on thermodynamic and kinetic properties of metal hydrides, the DSC-MS profile of as-milled $LiBH_4$ in this study is nearly the same as the pristine $LiBH_4$. It is speculated that this is because of the $LiBH_4$ size, which could not be decreased to the nano scale by ball milling. The slight influence of ball milling on accelerating the dehydrogenation properties of metal borohydride has also been reported in Li's study [32].

It is notable that all three endothermic events in the case of $LiBH_4$ + 9 mol% $NiFe_2O_4$ have been shifted to lower temperature compared with commercial and milled $LiBH_4$. The first endothermic peak at 102 °C is related to the orthorhombic to hexagonal structure transformation. The second one, accompanied by the major liberation of hydrogen in the MS profile, is associated with the interaction between $LiBH_4$ and $NiFe_2O_4$. The stronger and narrower hydrogen peak in the synchronous mass spectroscopy (MS) profile points to a rapid reaction. Considering the inferior amount of hydrogen and the melting temperature of commercial and as-milled $LiBH_4$, the bump after the second peak at 253 °C is assigned to the residual $LiBH_4$ fusion. The DSC-MS results are in good agreement with the non-isothermal measurements. Other gases emitted besides hydrogen are depicted in Fig. 4. Inset figures are magnified data for BH_3 and B_2H_6. Comparing emitted hydrogen, neither appreciable amounts of BH_3 or B_2H_6 are detected by MS during the heating process. This is encouraging, since it

usually poisons the fuel cells [33, 34] and is one of the reasons for the $LiBH_4$ cycling capacity loss [35, 36].

From the results discussed above, it can be seen that the decomposition behavior of $LiBH_4$ + 9 mol% $NiFe_2O_4$ is different from commercial $LiBH_4$. Herein, it is imperative to ascertain the reaction mechanism. The XRD analysis is used to analyze the phase transition after ball milling and dehydrogenation. XRD patterns of the samples after ball milling are shown in Fig. 5, along with commercial $LiBH_4$ for comparison. For commercial $LiBH_4$, there are no other peaks found, except those belonging to $LiBH_4$. As for the as-milled $LiBH_4$, the peaks of $LiBH_4$ are relatively broadened due to the reduction in particle size. There are no visible diffraction peaks of $LiBH_4$ in the pattern of as-milled $LiBH_4$ + 9 mol% $NiFe_2O_4$. To identify whether this is ascribed to the $NiFe_2O_4$ addition, XRD study of $LiBH_4$ + 3 mol% $NiFe_2O_4$ is conducted, as shown in Fig. 5 (d). Although the diffraction peaks of $LiBH_4$ are visible in $LiBH_4$ + 3 mol% $NiFe_2O_4$, their intensity is weaker than the as-milled $LiBH_4$. This means that the incremental content of $NiFe_2O_4$ causes gradual decrease in the intensity of $LiBH_4$ diffraction peaks and increases the degree of $LiBH_4$ amorphization [21]. It seems that there is no detectable reaction between $LiBH_4$ and $NiFe_2O_4$ during the milling process, since no other phases are identified except for $LiBH_4$ and $NiFe_2O_4$.

Fig. 6 shows the XRD patterns of the samples after dehydrogenation. Interestingly, for

the pure $LiBH_4$ after dehydrogenation, the $LiBH_4$ peaks are still observed. However, this is reasonable if sluggish $LiBH_4$ kinetics is considered, since only 2.4 wt% hydrogen is released when heated to 500 °C. In addition to $LiBH_4$, LiH and $LiBO_2$ are also detected, where LiH phases are produced from the decomposition of $LiBH_4$, while $LiBO_2$ phases come from the air contamination during measurements. In the case of $LiBH_4$ + 9 mol% $NiFe_2O_4$ sample, there are new diffraction peaks of $LiBO_3$, NiB, Fe_3O_4, and Fe_3B phases, caused by the interaction between $LiBH_4$ and $NiFe_2O_4$ during the dehydrogenation process. As Shan et al. [37] mentioned, most transition metal catalysts needs electrons to occupy the 3d orbit, and B has only one electron in the 2p orbit, while Fe and Ni have 6 and 8 electrons in the 3d orbit. Therefore, it is more feasible for B to provide an electron to Fe and Ni, achieving a more stable state. Herein, it is speculated that the destabilization effect of $NiFe_2O_4$ comes from the synergetic effects of NiB, Fe_3O_4 and Fe_3B.

Because of the limitations of XRD technique to detect amorphous or low content phases, Fourier transform infrared spectroscopy (FT-IR) is adopted to further reveal the reaction mechanism during the milling and de/re-hydrogenation process, as depicted in Fig. 7(a-b). Meanwhile, some dashed lines are added in Fig. 7 in order to better compare the peaks.

As seen in Fig. 7 (a), as-received $LiBH_4$ exhibits the characteristic peaks of B-H

stretching at 2387 cm^{-1}, 2295 cm^{-1} and 2225 cm^{-1}, and B-H bending at 1126 cm^{-1} [21, 26, 30, 38, 39]. The peak at 1633 cm^{-1} corresponds to O-H stretches, which may be related to the moisture contamination during examinations [13, 14] and the hygroscopicity of KBr (even when dehydrated) [25, 27, 40]. The shape of the as-milled $LiBH_4$ spectrum is the same as the pristine one, indicating that $LiBH_4$ phases remain stable during the ball milling process.

As for the $LiBH_4$ sample milled with 9 mol% $NiFe_2O_4$, the characteristic B-H peaks remain, but with some new subtle peaks at 985 cm^{-1}, 1173 cm^{-1}, 1281 cm^{-1} and 1325 cm^{-1}. The peak at 1281 cm^{-1} is B-H [30], which cannot be observed in the commercial $LiBH_4$, suggesting some other $LiBH_4$ phases. The peak at 1325 cm^{-1} is assigned to the vibration modes of the B-O bonds [41], pointing to partial interaction between $NiFe_2O_4$ and $LiBH_4$ during the milling process.

With respect to the samples after dehydrogenation in Fig. 7 (b), one can also find the same B-H peaks remaining in the case of as-received $LiBH_4$, compared to that before dehydrogenation, which further validates the XRD results. When it comes to the $LiBH_4$ + 9 mol% $NiFe_2O_4$ sample after dehydrogenation, it is found that all characteristic peaks of B-H stretching at 2387 cm^{-1}, 2295 cm^{-1} and 2225 cm^{-1} and B-H bending at 1126 cm^{-1} disappear, suggesting that $LiBH_4$ is completely decomposed. The fresh peaks at 745 cm^{-1} and 2455 cm^{-1} are attributed to $[B_{12}H_{12}]^{-1}$, indicating

$LiBH_4$ decomposition into $Li_2B_{12}H_{12}$ [28]. The FT-IR results confirm that $NiFe_2O_4$ can facilitate the decomposition of $LiBH_4$. Additionally, there is a partial reaction between $LiBH_4$ and $NiFe_2O_4$ during the ball milling process and $LiBH_4$ is partially reversed after the addition of $NiFe_2O_4$.

For better understanding of the potential destabilization mechanism, field scanning electron microscopy (FESEM) observations are conducted. Fig. 8 depicts FESEM images of the as-received, as-milled $LiBH_4$ and as-milled $LiBH_4$ + 9 mol% $NiFe_2O_4$. Prior to ball milling, the particle size of $LiBH_4$ ranges from 1 μm to 5 μm irregularly, posing a disadvantage to the dehydrogenation kinetics. For the commercial $LiBH_4$ after ball milling, the particles become much smaller, forming clusters, which also block rapid dehydrogenation. However, after ball milling with $NiFe_2O_4$, as shown in Fig. 8 (c), the particle size declines to 300 nm and 800 nm, and the distribution of these particles become more uniform. This may be one of reasons for the enhancement of dehydrogenation kinetics, as these nano-sized particles may serve as the nucleation sites. One thing should be noted that the embedded $NiFe_2O_4$ cannot be seen in the $LiBH_4$ matrix owing to its nano particle size.

From the above analysis, the superior destabilizing effects may result from the ball milling with $NiFe_2O_4$, leading to the significant $LiBH_4$ particle size decline.

Since the $NiFe_2O_4$ nanoparticles could not be observed by FESEM, it is imperative to

observe the nanostructure of un-doped and doped sample to further demonstrate the superior effects of nano-sized $NiFe_2O_4$. Fig. 9 shows dark field images, HRTEM and EDX analyses in the as-milled $LiBH_4$ + 9 mol% $NiFe_2O_4$ sample. In Fig. 9 (a) some black particles are homogenously distributed among the grey matrix. To figure out what these particles are, corresponding EDX measurements of the black area A and the grey area B are conducted, as shown in Fig. 9 (c) and (d), respectively. For the black area, O, Fe, Ni and Cu elements are identified (Cu comes from the sample holder). Although Fe and Ni elements are detected in the grey area, their intensity is much weaker than in the black area. It must be pointed out that EDX cannot reliably detect $LiBH_4$ due to the weak scattering of electrons by the light Li, B and H elements. Thus, it could be said that the black nanoparticles correspond to $NiFe_2O_4$, while the grey correspond to $LiBH_4$. It can be concluded that the $NiFe_2O_4$ nanoparticles are homogenously embedded in the $LiBH_4$ matrix after ball milling, improving rapid dehydrogenation kinetics.

$LiBH_4$ is detected by the FT-IR measurements, but not XRD, which was previously attributed to the amorphous state of $LiBH_4$ after ball milling with $NiFe_2O_4$. To demonstrate this, HRTEM images were obtained. As expected, there is some amorphization in the oval area, which is consistent with the FT-IR results and XRD analysis. The electron micrograph of dehydrogenated $LiBH_4$ + 9 mol% $NiFe_2O_4$ is shown in Fig. 10 (a), which looks similar to the as-milled sample with some

nanoparticles spread evenly among the grey areas. To further investigate the microstructure of $LiBH_4$ + 9 mol% $NiFe_2O_4$, selected area electronic diffraction (SAED) results are shown in Fig. 10 (b). The dim lattice diffraction pattern indicates that there is a high degree of amorphization, which can also be demonstrated by the broader XRD reflections. Additionally, the existence of Fe_3B and Fe_3O_4 phases are proven by the SAED measurements.

Conclusions

In this paper, it is found the nano-sized nickel ferrite ($NiFe_2O_4$) can effectively destabilize $LiBH_4$. According to the non-isothermal and isothermal desorption results, it liberates hydrogen at 89 °C and the hydrogen capacity is 10.75 wt% and one could get 5.49 wt% in just 20 minutes. In comparison with the raw $LiBH_4$, this is a huge advance. The mass spectroscopy detect neither BH_3 nor B_2H_6, which poison the fuel cells and can often lead to H_2 capacity loss, other than pure hydrogen. The XRD patterns combined with the SAED measurements uncover the existence of the Fe_3B, NiB and Fe_3O_4, which show a synergetic effect on accelerating the dehydrogenation properties of $LiBH_4$. The FT-IR results reveal that the addition of $NiFe_2O_4$ leads to the complete decomposition of $LiBH_4$ when heated to 500 °C, while there is still a big surplus of $LiBH_4$ for the un-doped one. The FESEM figures indicate that the particle size of $LiBH_4$ declines significantly after ball milling with $NiFe_2O_4$.

Acknowledgements

This study was supported by the Beijing Natural Science Foundation (2152019), and

the National Natural Science Foundation of China (Grant No. 51471054). Fuqiang Zhai thanks the China Scholarship Council (CSC) for providing the scholarship.

References

1. J. Yang and S. Hirano, *Adv. Mater.*, 2009, **21**, 3023-3028.

2. L. Schlapbach and A. Zuttel, *Nature*, 2001, **414**, 353-358.

3. J. Yang, A. Sudik, C. Wolverton and D. J. Siegel, *Chem. Soc. Rev.*, 2010, **39**, 656-675.

4. I. P. Jain, *Int. J. Hydrogen Energy*, 2009, **34**, 7368-7378.

5. S.-i. Orimo, Y. Nakamori, J. R. Eliseo, A. Züttel and C. M. Jensen, *Chem. Rev.*, 2007, **107**, 4111-4132.

6. A. Züttel, P. Wenger, S. Rentsch, P. Sudan, P. Mauron and C. Emmenegger, *J. Power Sources*, 2003, **118**, 1-7.

7. S.-i. Orimo, Y. Nakamori, G. Kitahara, K. Miwa, N. Ohba, S.-i. Towata and A. Züttel, *J. Alloys Compd.*, 2005, **404**, 427-430.

8. P. Sridechprasat, Y. Suttisawat, P. Rangsunvigit, B. Kitiyanan and S. Kulprathipanja, *Int. J. Hydrogen Energy*, 2011, **36**, 1200-1205.

9. L. A. Zeng, H. Miyaoka, T. Ichikawa and Y. Kojima, *J. Phys. Chem. C*, 2010, **114**, 13132-13135.

10. F. E. Pinkerton, M. S. Meyer, G. P. Meisner, M. P. Balogh and J. J. Vajo, *J. Phys. Chem. C*, 2007, **111**, 12881-12885.

11. D. M. Liu, W. J. Huang, T. Z. Si and Q. A. Zhang, *J. Alloys Compd.*, 2013, **551**,

8-11.

12. S. D. House, X. Liu, A. A. Rockett, E. H. Majzoub and I. M. Robertson, *The Journal of Physical Chemistry C*, 2014, **118**, 8843-8851.

13. R. Gosalawit-Utke, S. Meethom, C. Pistidda, C. Milanese, D. Laipple, T. Saisopa, A. Marini, T. Klassen and M. Dornheim, *Int. J. Hydrogen Energy*, 2014, **39**, 5019-5029.

14. T. Sun, J. Liu, Y. Jia, H. Wang, D. Sun, M. Zhu and X. Yao, *Int. J. Hydrogen Energy*, 2012, **37**, 18920-18926.

15. P. Ngene, M. H. W. Verkuijlen, Q. Zheng, J. Kragten, P. J. M. van Bentum, J. H. Bitter and P. E. de Jongh, *Faraday Discuss.*, 2011, **151**, 47.

16. D. Blanchard, Q. Shi, C. Boothroyd and T. Vegge, *J. Phys. Chem. C*, 2009, **113**, 14059-14066.

17. X.-D. Kang, P. Wang, L.-P. Ma and H.-M. Cheng, *Appl. Phys. A*, 2007, **89**, 963-966.

18. E. Callini, A. Borgschulte, C. L. Hugelshofer, A. J. Ramirez-Cuesta and A. Züttel, *J. Phys. Chem. C*, 2014, **118**, 77-84.

19. T. J. Frankcombe, *Chem. Rev.*, 2012, **112**, 2164-2178.

20. X. B. Yu, D. A. Grant and G. S. Walker, *J. Phys. Chem. C*, 2008, **112**, 11059-11062.

21. W. Cai, H. Wang, D. Sun, Q. Zhang, X. Yao and M. Zhu, *RSC Advances*, 2014, **4**, 3082.

22. P. Li, Z. Li, F. Zhai, Q. Wan, X. Li, X. Qu and A. A. Volinsky, *The Journal of Physical Chemistry C*, 2013, **117**, 25917-25925.

23. F. Zhai, P. Li, A. Sun, S. Wu, Q. Wan, W. Zhang, Y. Li, L. Cui and X. Qu, *The Journal of Physical Chemistry C*, 2012, **116**, 11939-11945.

24. P. Li, Q. Wan, Z. L. Li, F. Q. Zhai, Y. L. Li, L. Q. Cui, X. H. Qu and A. A. Volinsky, *J. Power Sources*, 2013, **239**, 201-206.

25. L. Guo, L. Jiao, L. Li, Q. Wang, G. Liu, H. Du, Q. Wu, J. Du, J. Yang, C. Yan, Y. Wang and H. Yuan, *Int. J. Hydrogen Energy*, 2013, **38**, 162-168.

26. J. Shao, X. Xiao, X. Fan, L. Zhang, S. Li, H. Ge, Q. Wang and L. Chen, *J. Phys. Chem. C*, 2014, **118**, 11252-11260.

27. Y. Zhao, L. Jiao, Y. Liu, L. Guo, L. Li, H. Liu, Y. Wang and H. Yuan, *Int. J. Hydrogen Energy*, 2014, **39**, 917-926.

28. Y. Yan, A. Remhof, S. J. Hwang, H. W. Li, P. Mauron, S. Orimo and A. Zuttel, *Phys. Chem. Chem. Phys.*, 2012, **14**, 6514-6519.

29. C. Frommen, M. Heere, M. D. Riktor, M. H. Sørby and B. C. Hauback, *J. Alloys Compd.*, 2015, DOI: 10.1016/j.jallcom.2015.01.113.

30. J. Chen, T. He, G. Wu, Z. Xiong, L. Liu, X. Ju and P. Chen, *J. Phys. Chem. C*, 2014, **118**, 13451-13459.

31. T. K. Nielsen, U. Bosenberg, R. Gosalawit, M. Dornheim, Y. Cerenius, F. Besenbacher and T. R. Jensen, *ACS Nano*, 2010, **4**, 3903-3908.

32. H. W. Li, K. Kikuchi, Y. Nakamori, K. Miwa, S. Towata and S. Orimo, *Scripta*

Mater., 2007, **57**, 679-682.

33. X. Si, F. Li, L. Sun, F. Xu, S. Liu, J. Zhang, M. Zhu, L.-Z. Ouyang, D. Sun and Y.-L. Liu, *J. Phys. Chem. C*, 2011, **115**, 9780-9786.

34. R. Gosalawit-Utke, J. M. B. von Colbe, M. Dornheim, T. R. Jensen, Y. Cerenius, C. B. Minella, M. Peschke and R. Bormann, *J. Phys. Chem. C*, 2010, **114**, 10291-10296.

35. X. Liu, D. Peaslee, C. Z. Jost, T. F. Baumann and E. H. Majzoub, *Chem. Mater.*, 2011, **23**, 1331-1336.

36. B. J. Zhang and B. H. Liu, *Int. J. Hydrogen Energy*, 2010, **35**, 7288-7294.

37. J. Shan, P. Li, Q. Wan, F. Zhai, J. Zhang, Z. Li, Z. Liu, A. A. Volinsky and X. Qu, *J. Power Sources*, 2014, **268**, 778-786.

38. P. Javadian, D. A. Sheppard, C. E. Buckley and T. R. Jensen, *Nano Energy*, 2015, **11**, 96-103.

39. B. J. Zhang, B. H. Liu and Z. P. Li, *J. Alloys Compd.*, 2011, **509**, 751-757.

40. M. P. Pitt, M. Paskevicius, D. H. Brown, D. A. Sheppard and C. E. Buckley, *J. Am. Chem. Soc.*, 2013, **135**, 6930-6941.

41. B. M. Concha, M. Chatenet, F. Maillard, E. A. Ticianelli, F. H. Lima and R. B. de Lima, *Phys. Chem. Chem. Phys.*, 2010, **12**, 11507-11516.

Figure captions

Fig. 1. Non-isothermal desorption curves of: (a) as-received $LiBH_4$, (b) as-milled $LiBH_4$ and as-milled $LiBH_4$ + (c) 3 mol%, (d) 5 mol%, (e) 7 mol%, (f) 9 mol%, and (g) 11 mol% $NiFe_2O_4$ nanoparticles.

Fig. 2. Thermal desorption curves of as-received $LiBH_4$ and as-milled $LiBH_4$ + 9 mol% $NiFe_2O_4$ at 300 °C and 200 °C.

Fig. 3. DSC-MS profiles of (a) as-received $LiBH_4$, (b) as-milled $LiBH_4$, (c) as-milled LiBH4 + 9 mol% $NiFe_2O_4$ at a heating rate of 5 °C min^{-1}. DSC profiles and MS spectra (m/z = 2) are shown as black and blue curves, respectively.

Fig. 4. Mass spectroscopy of (a): as-received $LiBH_4$ (b): as-milled $LiBH_4$ (c) as-milled $LiBH_4$ + 9 mol% $NiFe_2O_4$, inset figures are magnified images of m/z=13 and m/z=26. m/z=2, 13, 26 stands for H_2, BH_3, B_2H_6

Fig. 5. XRD patterns after high energy ball milling: (a) as-received $LiBH_4$, (b) as-milled $LiBH_4$, (c) as-milled $LiBH_4$ + 9 mol% $NiFe_2O_4$ (d) as-milled $LiBH_4$ + 3 mol% $NiFe_2O_4$.

Fig. 6. XRD patterns of the samples after dehydrogenation: (a) as-received $LiBH_4$ and (b) as-milled $LiBH_4$ + 9 mol% $NiFe_2O_4$.

Fig. 7. FT-IR spectra of (a): after milling (i) as-received $LiBH_4$, (ii) as-milled $LiBH_4$, (iii) as-milled $LiBH_4$ + 9 mol% $NiFe_2O_4$ and (b) after dehydrogenation (i) as-milled $LiBH_4$ (ii) as-milled $LiBH_4$ + 9 mol% $NiFe_2O_4$.

Fig. 8. FESEM images of (a) as-received $LiBH_4$ (b) as-milled $LiBH_4$ (c) as-milled $LiBH_4$ + 9 mol% $NiFe_2O_4$ and (d) is magnified image of (c).

Fig. 9. (a) TEM images and (b) HRTEM images of boundaries micrographs of black and grey regions. EDX: (c) black region and (d) grey region are results of as-milled $LiBH_4$ + 9 mol% $NiFe_2O_4$.

Fig. 10. (a) TEM micrograph and (b) corresponding SAED pattern of as-milled $LiBH_4$ + 9 mol% $NiFe_2O_4$ after dehydrogenation.

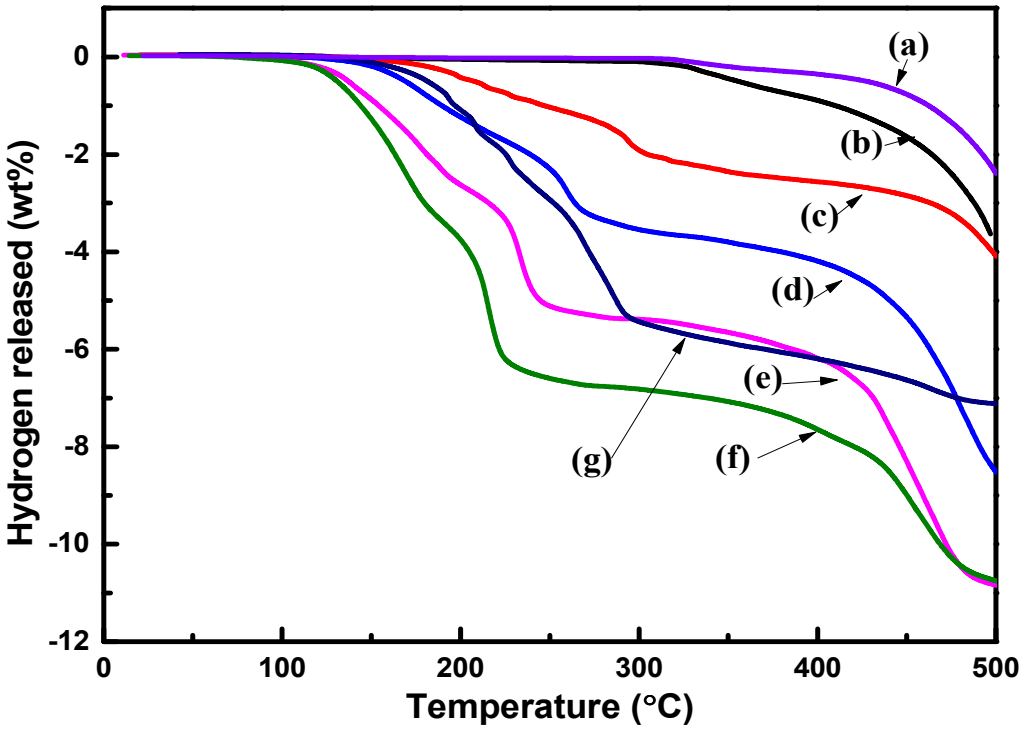
Hydrogen released (wt%)
0
-2
-4
-6
-8
-10
-12
0
100
200
300
400
500
Temperature (°C)
(a)
(b)
(c)
(d)
(e)
(f)
(g)

Fig. 1

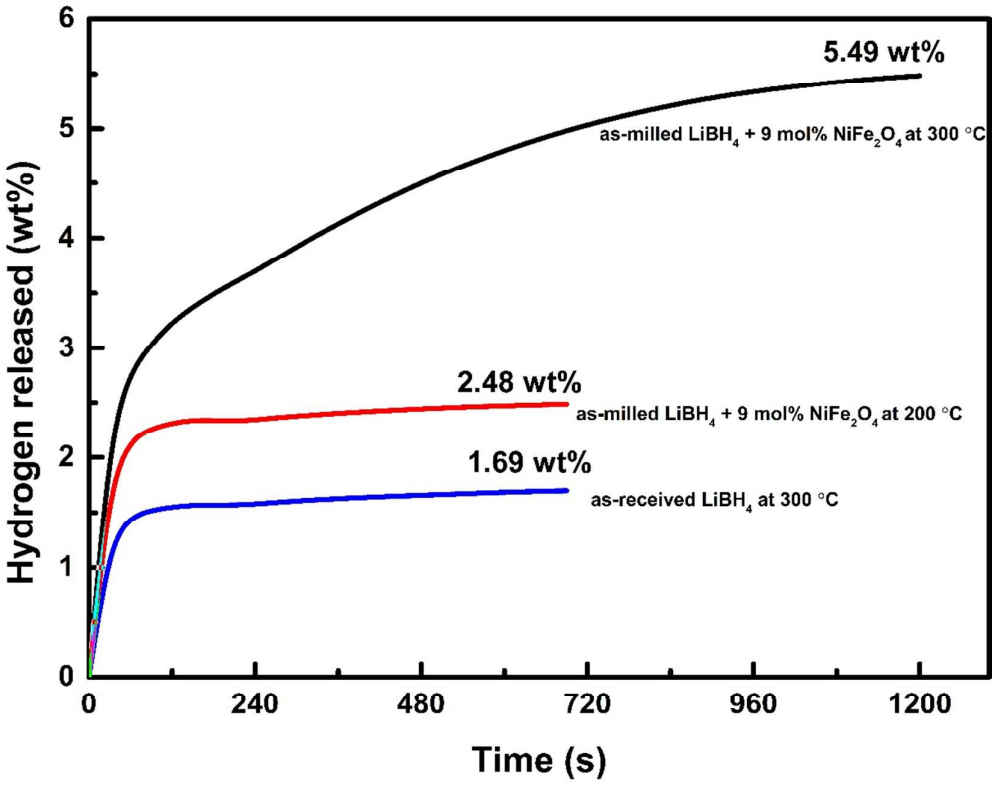
Hydrogen released (wt%)
Time (s)
0
1
2
3
4
5
6
0
240
480
720
960
1200
5.49 wt%
as-milled LiBH4 + 9 mol% NiFe2O4 at 300 °C
2.48 wt%
as-milled LiBH4 + 9 mol% NiFe2O4 at 200 °C
1.69 wt%
as-received LiBH4 at 300 °C

Fig. 2

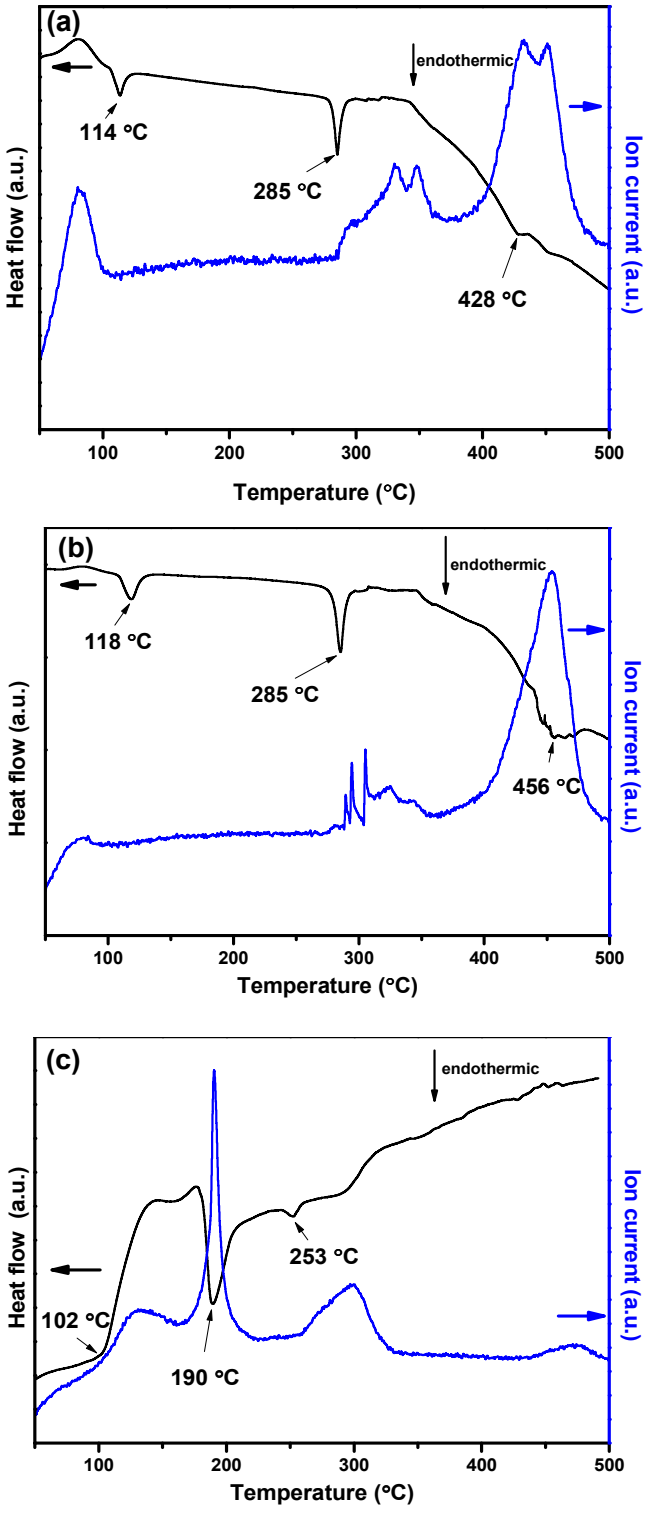
(a)
endothermic
114 °C
285 °C
428 °C
Heat flow (a.u.)
Ion current (a.u.)
100
200
300
400
500
Temperature (°C)
(b)
endothermic
118 °C
285 °C
456 °C
Heat flow (a.u.)
Ion current (a.u.)
100
200
300
400
500
Temperature (°C)
(c)
endothermic
253 °C
102 °C
190 °C
Heat flow (a.u.)
Ion current (a.u.)
100
200
300
400
500
Temperature (°C)

Fig. 3

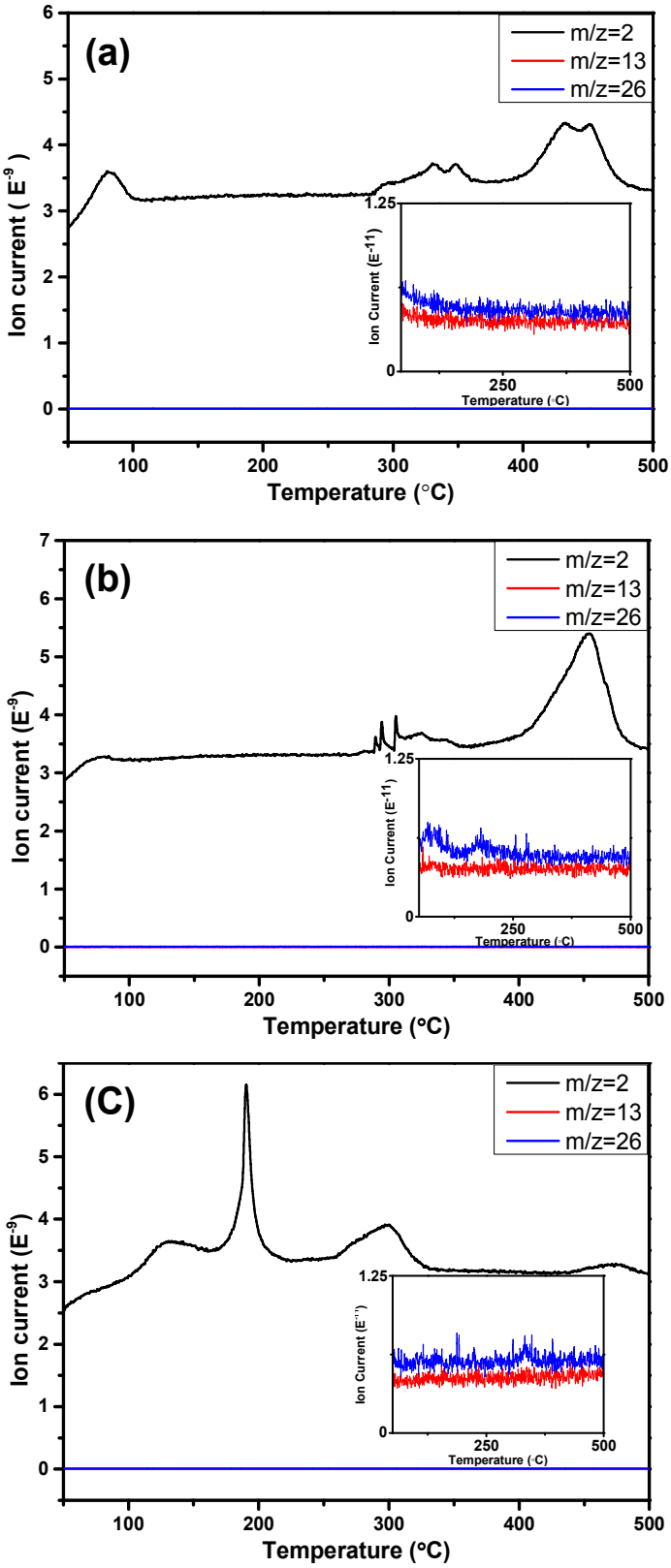
(a)
m/z=2
m/z=13
m/z=26
Ion current (E-9)
Temperature (°C)
Ion Current (E-11)
Temperature (°C)
(b)
m/z=2
m/z=13
m/z=26
Ion current (E-9)
Temperature (°C)
Ion Current (E-11)
Temperature (°C)
(C)
m/z=2
m/z=13
m/z=26
Ion current (E-9)
Temperature (°C)
Ion Current (E-11)
Temperature (°C)

Fig. 4

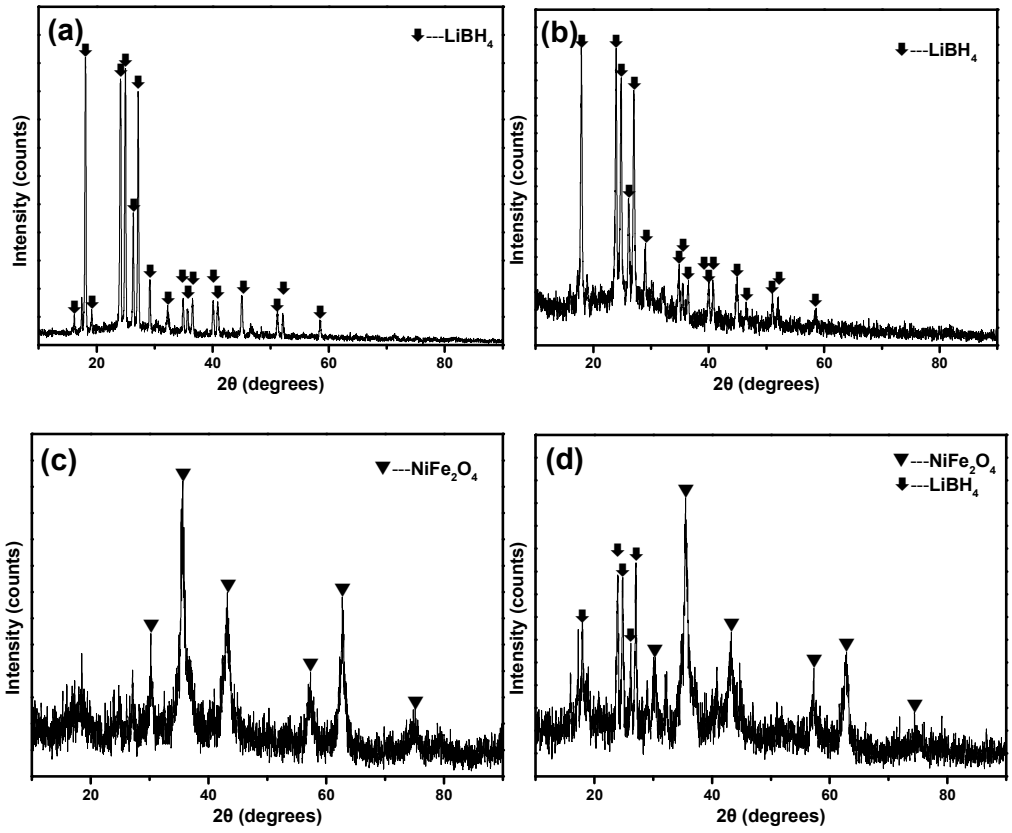
(a)
⬇---LiBH4
Intensity (counts)
20
40
60
80
2θ (degrees)
(b)
⬇---LiBH4
Intensity (counts)
20
40
60
80
2θ (degrees)
(c)
▼---NiFe2O4
Intensity (counts)
20
40
60
80
2θ (degrees)
(d)
▼---NiFe2O4
⬇---LiBH4
Intensity (counts)
20
40
60
80
2θ (degrees)

Fig. 5

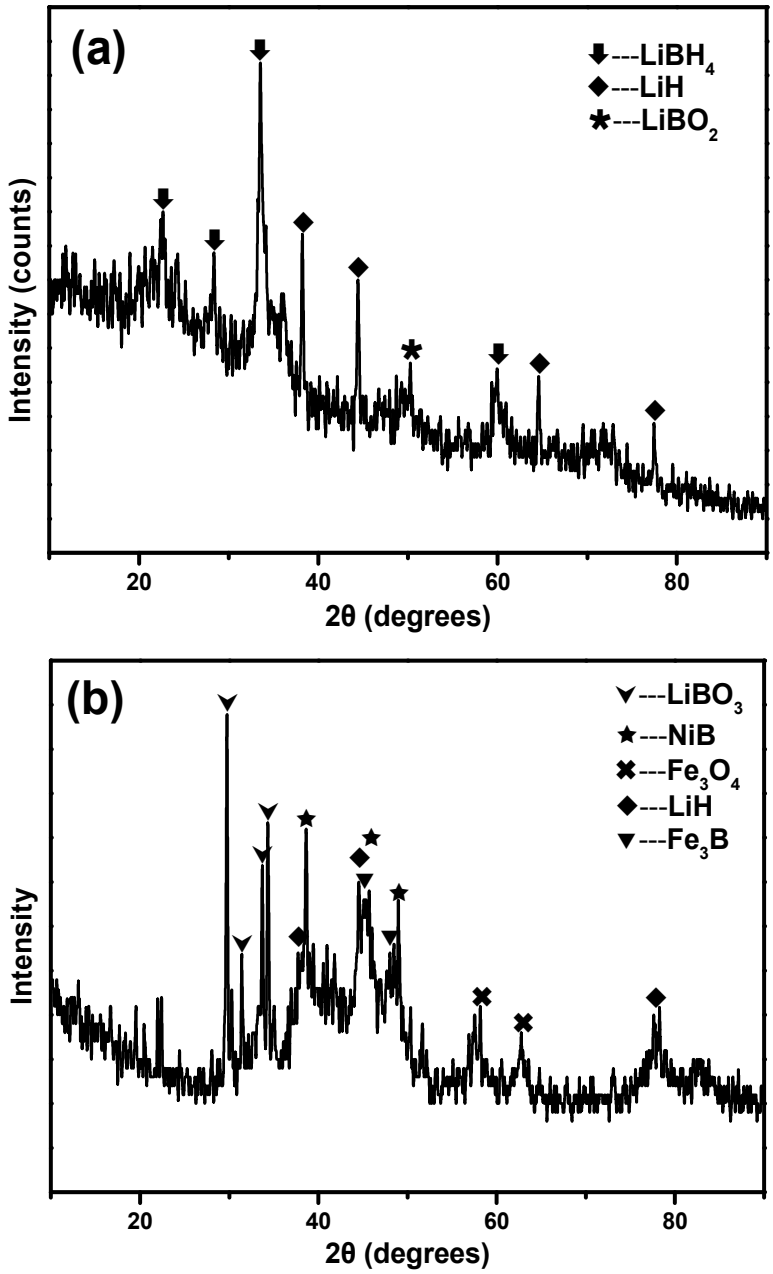
(a)
---LiBH4
---LiH
---LiBO2
Intensity (counts)
20
40
60
80
2θ (degrees)
(b)
---LiBO3
---NiB
---Fe3O4
---LiH
---Fe3B
Intensity
20
40
60
80
2θ (degrees)

Fig. 6

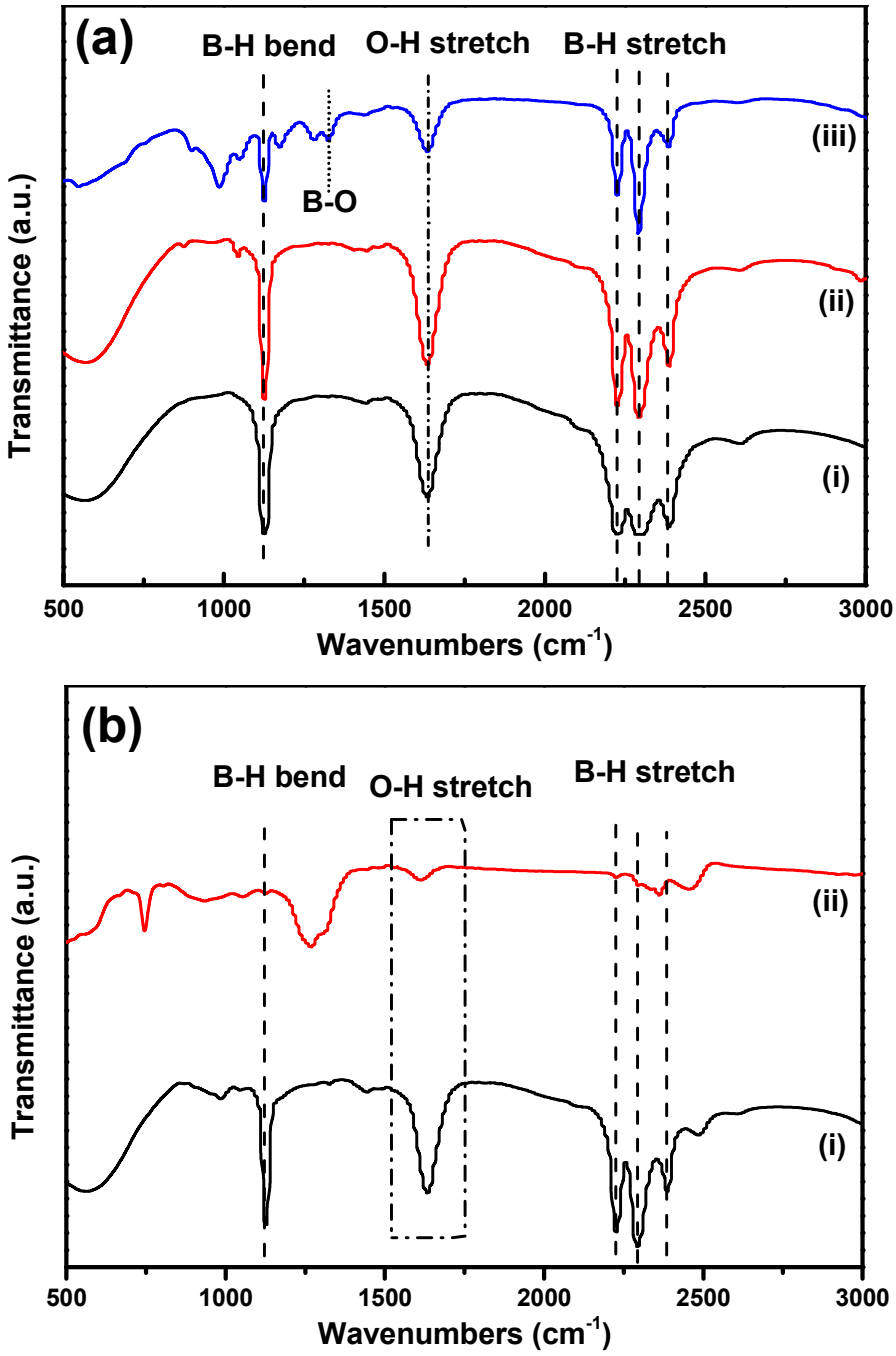
(a)
B-H bend
O-H stretch
B-H stretch
B-O
(iii)
(ii)
(i)
Transmittance (a.u.)
500
1000
1500
2000
2500
3000
Wavenumbers (cm-1)
(b)
B-H bend
O-H stretch
B-H stretch
(ii)
(i)
Transmittance (a.u.)
500
1000
1500
2000
2500
3000
Wavenumbers (cm-1)

Fig. 7

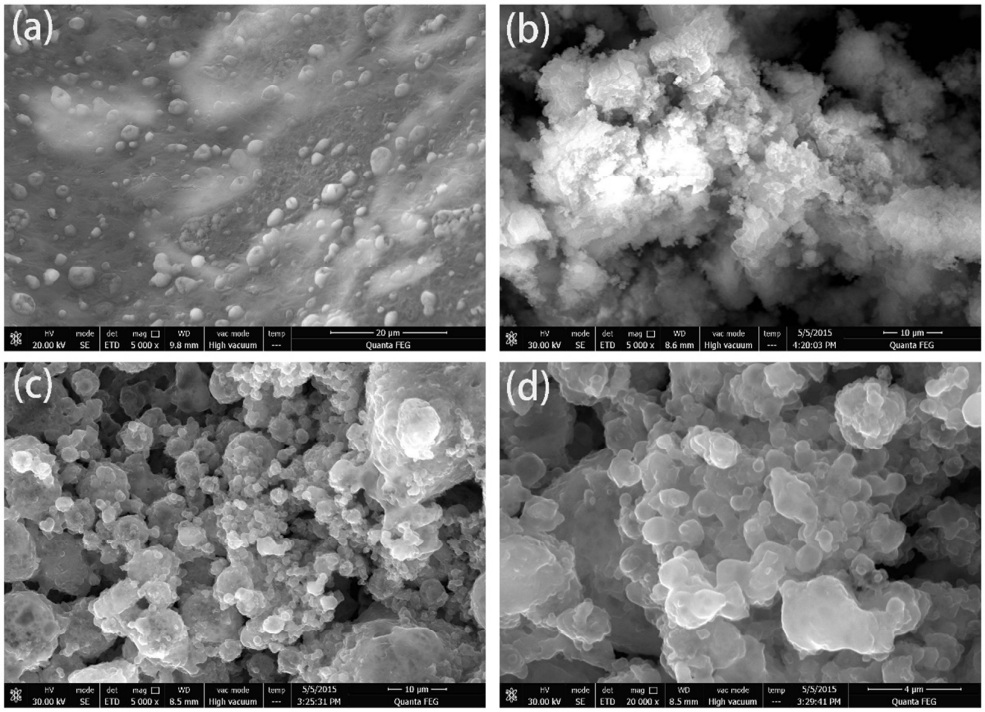
(a)
HV mode det mag WD vac mode temp
20.00 kV SE ETD 5 000 x 9.8 mm High vacuum ---
20 µm
Quanta FEG
(b)
HV mode det mag WD vac mode temp 5/5/2015
30.00 kV SE ETD 5 000 x 8.6 mm High vacuum --- 4:20:03 PM
10 µm
Quanta FEG
(c)
HV mode det mag WD vac mode temp 5/5/2015
30.00 kV SE ETD 5 000 x 8.5 mm High vacuum --- 3:25:31 PM
10 µm
Quanta FEG
(d)
HV mode det mag WD vac mode temp 5/5/2015
30.00 kV SE ETD 20 000 x 8.5 mm High vacuum --- 3:29:41 PM
4 µm
Quanta FEG

Fig. 8

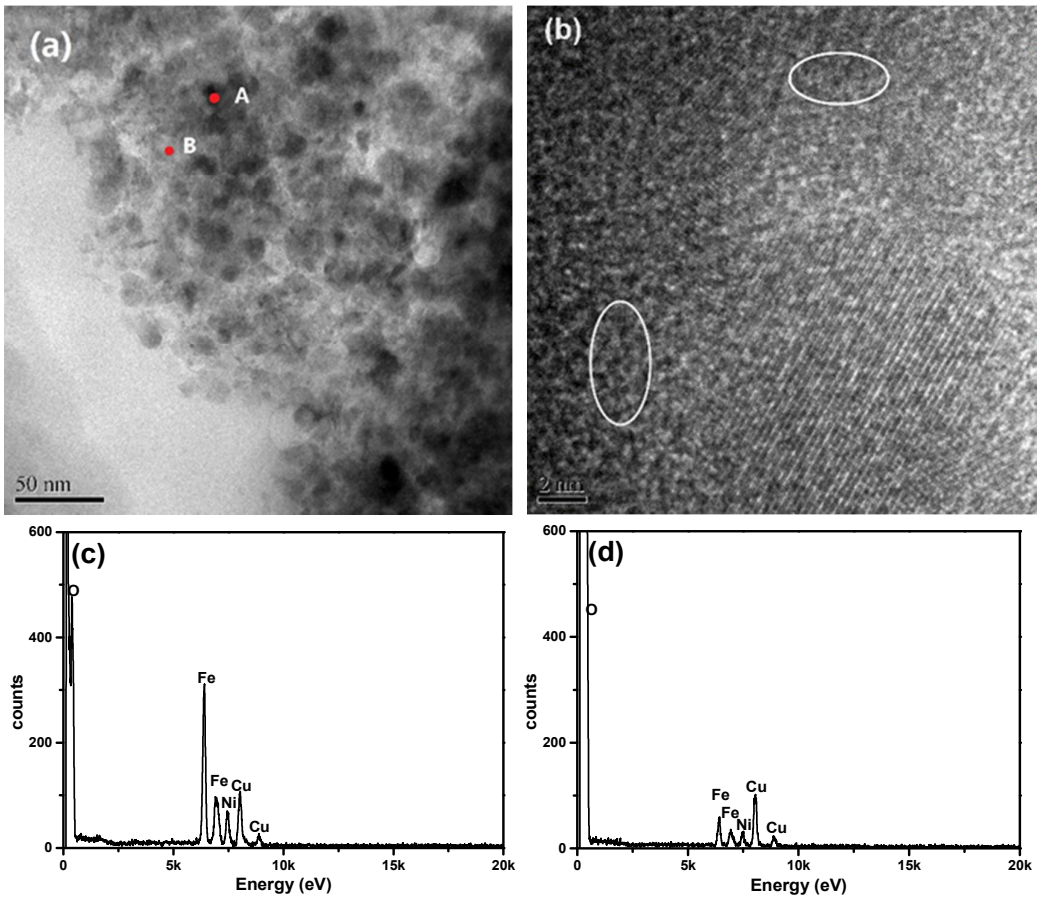
(a)
A
B
50 nm
(b)
2 nm
(c)
O
Fe
Fe
Ni
Cu
Cu
counts
Energy (eV)
(d)
O
Fe
Fe
Ni
Cu
Cu
counts
Energy (eV)

Fig. 9

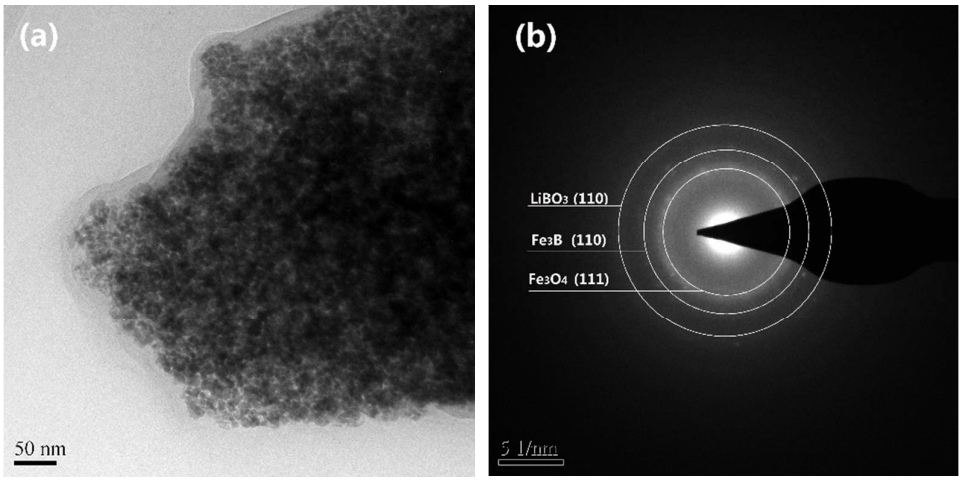

Fig. 10